Enhanced Composite Plate Impact Damage Detection and Characterisation using X-Ray Refraction and Scattering Contrast Combined with Ultrasonic Imaging

D. Shoukroun[1,4], L. Massimi[1], F. Iacoviello[2], M. Endrizzi[1], D. Bate[3], A. Olivo[1], P. Fromme[4]

[1] Department of Medical Physics and Biomedical Engineering, University College London, WC1E 6BT, UK

[2] Department of Chemical Engineering, University College London, WC1E 6BT, UK

[3] Nikon, X-Tek Systems Ltd., Tring, Hertfordshire, HP23 4JX, UK

[4] Department of Mechanical Engineering, University College London, WC1E 6BT, UK

Contact Author: D. Shoukroun, dana.shoukroun.17@ucl.ac.uk

Abstract

Ultrasonic imaging and radiography are widely used in the aerospace industry for non-destructive evaluation of damage in fibre-reinforced composites. Novel phase-based X-ray imaging methods use phase effects occurring in inhomogeneous specimens to extract additional information and achieve improved contrast. Edge Illumination employs a coded aperture system to extract refraction and scattering driven signals in addition to conventional absorption. Comparison with ultrasonic immersion C-scan imaging and with a commercial X-ray CT system for impact damage analysis in a small cross-ply carbon fibre-reinforced plate sample was performed to evaluate the potential of this new technique. The retrieved refraction and scattering signals provide complementary information, revealing previously unavailable insight on the damage

extent and scale, not observed in the conventional X-ray absorption and ultrasonic imaging, allowing improved damage characterisation.

Keywords: B. Impact behaviour; D. Non-destructive testing; D. Radiography; D. Ultrasonics

1. Introduction

Carbon fibre-reinforced composites are widely used in the aerospace industry as they offer high strength to weight ratios [1]. However, carbon fibres are brittle, and carbon fibre-reinforced composites are prone to Barely Visible Impact Damage (BVID) [2]. Matrix cracking is typically the initial type of BVID to occur and thus the most common for transverse impacts [3]. Different types of crack can form (e.g., shear, bending cracks), depending on the stresses involved. Delaminations are initiated by transverse impact and are the most severe type of BVID [2]. Such defects affect the structural integrity of the composites, potentially leading to complete failure. The detection and identification of such defects is important for predicting the composite structure health and performance capabilities. In the aerospace industry, carbon fibre-reinforced polymers (CFRP) have a permitted 0.4% compressive strain to failure, and as a result the cost of maintenance and inspection of the parts is high [4].

Different Non-Destructive Evaluation (NDE) techniques can be used for the monitoring of composites, including ultrasonic imaging, radiography, eddy current testing, magnetic and thermographic testing [5-7]. Fast, accurate and cost-effective techniques are required, with radiographic CT and ultrasonic imaging the main techniques used today in the aerospace industry [8]. Immersion ultrasonic testing allows for automated scanning of a specimen with uniform coupling, and thus sensitivity, as well as the possibility of scanning irregular shapes and surfaces [8]. Immersion ultrasonic C-scans are used for the detection of defects and delaminations in the normal plane, whereas cracks oriented parallel to the emitted waves are unlikely to be observed [9]. Automated ultrasonic NDE systems for the detection of manufacturing defects in composites such as voids, irregular fibre volume fraction, ply stacking sequence, fibre waviness, and out-of-plane fibre wrinkling were developed [10, 11]. The main disadvantage of ultrasonic imaging is its resolution limitation, as the signal attenuation increases with increasing frequency, thus requiring a trade-off between resolution and inspection depth. Small features such as micro-defects or individual fibres cannot be resolved in composite plates using ultrasonic imaging. Another disadvantage of ultrasonic C-scan imaging is its limitation for the detection of multiple defects across the thickness of the sample, as a large fraction of the signal reflects or scatters at the first defect [9].

In conventional X-ray imaging, the absorption rate of X-rays depends on the attenuation coefficient and thickness of the features studied, hence large enough features present in a composite plate can be observed as variations in the detected intensity due to the fraction of X-rays absorbed [8]. X-ray computed tomography (CT) is the most commonly used imaging technique for the detection of defects in composite plates, such as delaminations, porosity and cracks, which are not visible in 2D images [12]. Ultrasonic C-scans are often used to prove the viability of new CT reconstruction methods or experimental setups [13]. Comparisons involving radiographic imaging and ultrasonic imaging techniques were performed to study the evolution of damage (cracks, delaminations) in self-healing composites [14], for the detection of BVID in composites (e.g. matrix and fibre cracks, debonding and fibre pullout) [15], as well as the evaluation of porosity content in composites plates, which is more difficult to estimate using ultrasonic imaging alone [16]. Both imaging methods are capable of detecting damage in fibre-reinforced composite plates, with X-ray CT imaging offering higher resolutions and capable of detecting micro-damage and individual plies, up to the detection of individual fibres [13–15].

For defects in composite materials too small to cause sufficient variation in the detected intensity and invisible using conventional radiography, X-ray Phase Contrast imaging (XPCi) offers an advantageous alternative. XPCi is different from conventional X-ray imaging as it relies on the phase shift of the X-ray wave front caused by inhomogeneities in the sample, as opposed to absorption in conventional X-ray imaging. Edge Illumination (EI) XPCi is a differential phase imaging technique that uses a coded aperture system to translate the change in the X-ray propagation direction that accompanies the phase effects into a variation in the detected intensity [17]. With the acquisition of at least three projection images, this method allows for the simultaneous retrieval of standard absorption, refraction, in which the pixel intensity represents the refraction angle of the beam, and scattering images: the latter are a complementary representation of the microscopic structure of the imaged sample, which highlights ultra-small angle scattering caused by features in the sub-pixel scale [18]. Several other XPCi imaging techniques exist, e.g., Talbot-Lau grating interferometry was used to investigate impact damage in composite plates [19]. However, EI offers several advantages in terms of practical implementation in fast, large field of view, and vibration-resistant industrial systems [20].

XPCi of composite plates performed using synchrotron radiation was observed to be sensitive to variations in homogeneity [21], and enabled the detection of cracks in macro-fibres and voids to much higher standards than conventional radiography [22]. Talbot-Lau grating interferometry XPCi was used to characterise the weave pattern, size of fibre bundles, and resin contents of pre-preg CFRP samples [19]. The Talbot-Lau approach was also used for the study of fibre orientation in short glass fibre reinforced composites using the direction-dependent properties of ultra-small-angle scattering [23].

Limited research has compared ultrasonic and X-ray phase contrast imaging techniques for damage detection in fibre-reinforced composite plates. Gresil et al. [24] used immersion through-transmission imaging and phased array pulse echo imaging to benchmark Talbot-Lau grating interferometry XPCi as a viable NDE technique. Measuring porosity in pre-preg CFRP samples, they concluded that XPCi offered a much better quantification than ultrasonic phased array or through-transmission techniques. Characterisation of low velocity impact damage in a cross-ply composite plate was performed using both ultrasonic C-scan imaging and EI XPCi. It was shown that the phase-enhanced and scattering images presented an advantage for the detection of small defects (tens of μm and below), as opposed to the ultrasonic C-scan imaging, which was capable of detecting macro-defects such as delaminations (100 μm and above) [25].

In this contribution, EI XPCi and ultrasonic C-scan imaging were used to assess the damage in a small pre-preg CFRP specimen with impact damage, and compare the features observed using the two imaging methods. EI XPCi CT scans and ultrasonic C-scans of the sample were taken, and the images were qualitatively analysed, to identify and quantify the extent and nature of the observed damage, as well as any additional feature revealed by EI XPCi. Confirmation of the observed features was achieved using a commercial high-resolution X-ray CT scan.

2. Experiments

A 2 mm thick, 19 mm x 19 mm carbon fibre/epoxy resin cross-ply laminate sample containing severe impact damage was imaged. The 16 plies were measured to be approximately 150 μm thick, and the top and bottom laminae had a woven structure. The sample contained an indent induced by impact, approximately 4 mm in diameter and 1.2 mm in depth, which resulted in a small protrusion on the back of the plate, approximately 5.5 mm in diameter and 0.5 mm thick, as shown in Fig. 1.

Ultrasonic immersion C-scans were performed using a ¼ inch (6mm) diameter, focused longitudinal 20MHz transducer. The transducer was mounted on a computer-controlled scanning rig, perpendicular to the surface of the sample (Fig. 2). The transducer was positioned at the focal length of ¾ inch (19mm) above the surface of the sample. A pulser/receiver (Panametrics 5601T) was used to drive the transducer and amplify the pulse-echo signal. For each scan point the full A-scan was acquired and saved to MATLAB using a digital storage oscilloscope (LeCroy 9304) with a sampling frequency of 100 MHz. A 10mm thick steel plate was placed at the bottom of the water tank and the composite sample was placed 3 mm above the surface of the steel plate, as shown in Fig. 2, to allow for double-through transmission signals to be recorded. The scans were performed over an area of 130 by 130 steps, with a 200 μm step size in both the width and length directions, to contain the full sample. The scanning time was about

8 hours on a laboratory system. The transducer focal spot was calculated to be 280 μm, the wave velocity was estimated as 1380 m/s, corresponding to 70 μm wavelength. The A-scans at different lines along the sample were used to generate B-scan visualizations for comparison with EI XPCi CT slices.

The experimental setup used to acquire EI XPCi CT images of the sample included a Rigaku MicroMax 007 HF rotating anode molybdenum X-ray source, with a 70 μm focal spot, used at 40 kVp and a current of 20 mA. The detector used was a Hamamatsu C9732DK flat panel CMOS detector with a 50 x 50 μm^2 pixel size. Due to cross-talk between neighbouring detector pixels caused by the diffusion in the scintillator, the effective resolution of the detector was approximately 100 μm [26]. EI XPCi was implemented using a set of coded aperture systems (masks): a first mask, referred to as the sample mask, was placed upstream of the imaged sample, splitting the divergent beam into an array of individual beamlets (Fig. 3). The sample mask had an aperture of 12 μm and a period of 38 μm, with the source to sample mask distance (Z_{SM}) of 0.65 m and 0.05 m upstream of the sample stage (Z_{OM}). A second mask, referred to as the detector mask, was placed in contact with the detector, making the regions separating adjacent pixels insensitive to incoming X-rays. The detector mask had a 20 μm aperture and a 48 μm period, and the source to detector distance (Z_{SD}) was 0.85 m. The system magnification was calculated to be 1.25. The masks were made of gold on a graphite substrate and were manufactured by MicroWorks. The resulting system was only sensitive to the phase effects in the x-direction, where a gradient in the refractive index of the sample results in the refraction of the beamlets and thus leads to a change in the detected intensity [17].

The CT image acquisition process included the acquisition of the illumination curve (typically assumed to be a Gaussian), which represents the variation of the detected intensity as a function of the sample mask position relative to the detector mask position [17]. Five relative mask positions, translating the sample mask along the x-direction in sub-pixel steps of 6 μm, were used during the CT acquisition to minimise the scan time. 5 sets of 1800 projections, with a rotation of 0.2° per projection, were taken at each mask position. Each projection had 1.2s exposure time, resulting in an overall acquisition time of 12 hours (3 hours live scanning time) due to overheads in the non-optimised system. The voxel size was $(41\ \mu m)^3$. Phase retrieval was carried out on the image sequence to obtain the absorption, refraction, and scattering projection images, which were then reconstructed using a CT reconstruction algorithm provided by Nikon.

The standard phase retrieval method, discussed in [18], fits a Gaussian distribution to the measured intensity of each pixel in the images with the sample. The Gaussians were then compared to the correspondent Gaussians fitted without the sample, as shown in Fig. 4. The absorption images were retrieved from the decrease in amplitude (A_0 to A_1), the refraction images from the change in the centre position of the Gaussian, and the scattering images from the change in the width of the Gaussian, caused by ultra-small-angle scattering [18]. To take the cross-talk between neighbouring apertures into account, a new phase retrieval method was used [27], which involves fitting three overlapping Gaussian distributions, and using the coefficients of the central Gaussian for the phase retrieval. The reconstructed CT images were then segmented and visualised using Drishti, a volume exploration and presentation tool [28].

An additional high resolution X-ray scan of the sample was performed using a commercial X-ray system (Nikon XTEK XTH 225kV). The scan was performed using 40kV beam energy, 358µA beam current and a power of 14.3W. A PerkinElmer 1620 flat panel detector was used, with 200µm pixel size. The system had a geometric magnification of 14 resulting in an effective pixel size of 14µm. The exposure time per projection was 1s, and a total of 3185 projections were acquired, resulting in a scanning time of approximately 1 hour. The experimental setup for this system is described in [29].

3. Results and Discussion

The results obtained from the ultrasonic C-scans and EI XPCi CT scans are presented as slices taken from different cross-sections of the sample. For each cross-section, two B-scans are presented with, respectively, the front and back surface of the sample facing the transducer, with the front surface containing the indent, and the back surface the protrusion. Three retrievals (absorption, refraction and scattering) are shown for the matching CT slice, as well as an RGB image, which is the superposition of the three retrieved images, with absorption in blue, refraction in green and scattering in red. Three sets of figures are shown, one from an undamaged area of the sample, one showing a delamination across the sample, and one from the most severely damaged part of the sample.

3.1 Undamaged Part

For an undamaged part of the composite sample, the ultrasonic B-scans (Fig. 5a/b) and the X-ray images (Fig. 5d/f) show reasonably uniform ply layers. The ultrasonic

B-scan images show strong reflection from the surface and back wall, with weaker reflections from the inner plies. Due to surface unevenness, the reflection from the front (impact side, Fig. 5a) is larger and more irregular than that from the back surface (Fig. 5b). The reflections from the inner plies in both B-scans indicate reasonably homogeneous and aligned plies, but potentially with some waviness.

The matching X-ray absorption CT slice (Fig. 5d) shows contrast due to the cross-ply layup of the sample, with regular plies visible. The contrast can be enhanced (Fig. 5g) for the uneven sample surfaces to be observed better. Plies are clearly defined, with a signal from the ply interfaces visible in the refraction image (Fig. 5e), with the intensity of the intra-ply area matching the background grayscale. This points toward a homogeneous distribution of plies and ply alignment. This homogeneity is more clearly visible in the 3D rendering of the refraction signal in Fig. 5h, where the contrast was adjusted to highlight the interfaces in the sample, resulting in a strong signal from the surfaces of the sample and a lack of signal from the intraply area within the sample. The only visible signal is due to the impact damage at the center of the sample, as opposed to the inhomogeneities from the ply structure.

The scattering images (Fig. 5f/i) show clear signals from the ply layer interfaces, suggesting small, sub-pixel inhomogeneity. Figure 5e/f shows some imaging artefacts in the CT reconstruction at the specimen edges due to the specimen shape. The 3 X-ray retrieved images were superimposed in Fig. 5j to highlight the complementarity of the signals. For the undamaged part of the sample, the edges are clearly visible, and an indication of the ply layers can be observed from the absorption (blue) and scattering signal (red).

3.2 Delamination

Figure 6 shows a cross-section about 5 mm from the impact center, where no indent can be observed. Delamination is detected by the ultrasonic B-scan and X-ray images close to the bottom of the sample. The delamination was localized between plies 14 and 15 from the X-ray images, in agreement with the ultrasonic B-scan images, as the first reflection from the delamination in both scans was found to be approximately 0.3 mm from the back surface of the sample, which corresponds to the thickness of the two plies. In the B-scans, a strong reflection was observed (Fig. 6a/b), characteristic of a delamination [9]. From the X-ray retrievals, the delamination length at that location was measured to be approximately 5 mm in length from the absorption and refraction images. This was in good agreement with the measurement of approximately 5.5 mm from the ultrasonic B-scan, considering the system resolution (0.2mm step size).

In the slices and the 3D rendering of the X-ray images, the delamination is visible in all three retrievals, with the absorption images showing a separation between the plies (Fig. 6d, with stretched contrast in Fig. 6g). A strong signal is observed in the refraction retrieval (Fig. 6e/h) due to the interface created between the delamination and the neighbouring plies. A strong scattering signal is also observed around the delamination (Fig. 6f/i), indicating the presence of the sub-pixel damage. Identification of the features observed in the scattering signal is not directly achievable, but it could indicate that either the delamination (ply-separation) extends further than observed in the absorption and refraction signal (Fig. 6j), or additional micro-damage e.g. debonding, micro-matrix cracks, or fibre damage. These features are better visible in the

3D renderings shown in Fig. 6h/i with enhanced contrast to highlight the interfaces of the delamination in the refraction signal and the surrounding damage in the scattering image, respectively. These micro-features are unique to the scattering signal and offer a more accurate representation of the possible damage extent, which could not be observed in the other signals due to the scale of those features. The complementarity of the scattering signal allows to observe features of different magnitudes and nature and thus to better understand the defects present in the sample. The 2-dimensional cuts through the 3D rendering of the X-ray signals (Fig. 7) shows that the delamination is not complete, but is shaped as a ring around the impact damage which pushed the central part of the specimen downwards and caused the protrusion. The refraction and scattering renderings show in addition to the main delamination towards the back of the specimen, smaller interfaces and delaminations within the protrusion.

3.3 Center of Damage

The impact caused damage across the sample, as can be seen from both the ultrasonic B-scans (Fig. 8a/b), and the X-ray images across the impact center. The ultrasonic B-scans exhibit one of the limitations of ultrasonic testing for damage detection in composite plates. The indented front surface and protrusion cause strong reflections and scattering, with potentially unobserved internal defects due to lack of signal past the damage closest to the surface. An example of such a situation is observed here, where a crack across the thickness of the sample was only observed in the X-ray images (Fig. 8). The macro-crack was observed in all three X-ray retrievals, however they indicate different features; the absorption CT slice (Fig. 8d) shows clear damage in the sample, with the crack and further damage better visible with enhanced contrast (Fig. 8g). The refraction signal (Fig. 8e/h) highlights the interface of the crack through the sample, whereas the scattering signal (Fig. 8f/i) indicates further micro-damage in the sample surrounding the crack. This level of accuracy in the measurement of the damage extent is unachievable using ultrasonic imaging or conventional attenuation-based CT alone, represented here by the retrieved absorption images (Fig. 8d).

Moreover, a clear scattering signal can be observed throughout the damaged area of the sample. The presence of signal in the different retrievals indicates the presence of different types of damage (Fig. 8j). The signal in the refraction images is due to the small voids created by the separation of plies in the inter-ply area originating from the material being displaced when the damage occurred, as shown in Fig. 8k. The scattering signal is due to the micro-damage that occurs within the plies due to the material displacement. The multimodal imaging of the sample, as well as the superposition of all three retrievals in an RBG image, as shown in Fig. 8j/k, thus allows to locate and clearly visualise the damage, as well as identify the scale of damage involved and have a more accurate representation of the extent of the damage from the refraction and scattering images to complement the absorption and ultrasonic images.

3.4 Quantification of damage extent and comparison with high-resolution X-ray absorption CT scan

A quantification of the damage extent was achieved using a 2D projection of the CT slices through the specimen thickness for all three X-ray signals, effectively adding the damage indications to visualize the overall damage extent. It can be observed that in the absorption 2D projection (Fig. 9a) the damage appears round-shaped, similar to the shape observed in the double through transmission ultrasonic C-scan (Fig. 9g). However, the refraction and scattering signal show a more square-shaped damage indication (Fig. 9c/e), due to the types of defects observable in these signals. Profile plots were taken across the 2D projections of the sample in order to assess the damage extent across the damaged area of the sample. Examples of such profile plots are shown in Fig. 9b/d/f/h, corresponding to the red lines in the 2D projections. A simple thresholding method was used to assess the extent of the damage. It was measured to be approximately 5.9 x 5.4 mm^2, 5.9 x 5.7 mm^2 and 6.6 x 7.3 mm^2 for the absorption, refraction and scattering signals, respectively. As expected, the scattering signal indicates a larger damage extent than the absorption and refraction signals, due to its sensitivity to sub-pixel features. The dimensions observed in the double-through transmission C-scan of the sample were calculated to be approximately 6.7 x 7.1 mm^2, comparable to the size obtained from the scattering signal.

The features observed in the EI XPCi signals were compared to a high resolution X-ray CT scan performed using a commercial system with voxel size of $(14\mu m)^3$. The higher resolution absorption scan (Fig. 10b) confirms the features observed from the lower resolution absorption (Fig. 10a), refraction, and scattering signals. This is more clearly visible in Fig. 10c/d, where the respectively the refraction and scattering signals were superimposed on the high resolution absorption scan. The interfaces observed in the refraction signal are confirmed by the high resolution scan (Fig. 10c arrows). The presence and extent of those interfaces confirms our interpretation as to the nature of the refraction signal. Small voids created between the plies, not visible in the low resolution absorption scan (Fig. 10a), became visible in the high resolution absorption scan (Fig. 10b), and match the superimposed scattering signal (Fig. 10d). The scattering signal extends beyond the damage visible in the high resolution scan in certain areas, suggesting that an even higher resolution scan would be needed to observe these features. This confirms our hypothesis that the scattering signal indicates micro-damage at a scale below the resolution of the imaging system.

4. Conclusions

A qualitative comparison between ultrasonic immersion C-scan imaging and EI XPCi images was performed on a small, cross-ply composite sample with severe impact damage to investigate the different features observable using the two imaging techniques. Standard ultrasonic C-scan imaging allowed the detection and sizing of the overall damage. The delamination close to the bottom layer was accurately sized with good contrast from the C-scans. However, two main limitations of ultrasonic scanning were observed. Good penetration depth and a clear reflection of the respective back wall was seen, but the chosen ultrasonic frequency (20 MHz) corresponded to a wavelength comparable to the ply layer thickness. Together with a non-smooth sample surface, this made accurate measurement of ply layer thickness and waviness difficult. The second limitation can be seen in Fig. 6a/b and Fig. 8a/b, where strong reflections at large defects (e.g. delamination) prohibited the detection of additional, internal defects.

EI XPCi resolves some of these limitations by offering a higher resolution as well as visualisation of the full sample. As a result, EI XPCi allows the detection of internal defects and features that are not visible using ultrasonic imaging, more specifically in this case, a crack through the thickness of the sample. The multimodal imaging using EI

XPCi, resulting in the retrieval of absorption, refraction and scattering images of the sample, contributes to the identification of the defects occurring in the damaged area. The refraction signal highlights interfaces due to the separation of plies (small voids and delaminations), and the scattering signal corresponds to sub-pixel features which indicate micro-damage accompanying the main defects. Combining the features observed from the different X-ray retrievals, an accurate estimation of the damage extent can be obtained from a low resolution system relative to ultrasonic imaging or higher resolution conventional radiography. Based on the physics of the different signals, some assessment of the detected damage type can be obtained, but below the system resolution only the presence of damage can be obtained from the scattering signal. However, EI XPCi CT imaging currently has some limitations, as the scanning times are long and, similar to conventional CT imaging, the sample must be small enough to be contained in the field-of-view. This could be resolved by scanner acquisition optimisation and by the introduction of computed laminography for further investigations.

Declaration of interest: None.

Funding: This work was supported by the UK Engineering and Physical Sciences Research Council (EPSRC) [grant number EP/N509577/1] and Nikon UK Ltd. M. Endrizzi was supported by the Royal Academy of Engineering under the RA Eng. Research Fellowship scheme. A. Olivo was supported by the Royal Academy of Engineering under the RA Chairs in Engineering Technology scheme.

References:

[1] Staszewski WJ, Mahzan S, Traynor R. Health Monitoring of Aerospace Composite Structures - Active and Passive Approach. Compos Sci Technol 2009;69:1678–85. https://doi.org/10.1016/j.compscitech.2008.09.034.

[2] Richardson M, Wisheart M. Review of Low-velocity Impact Properties of Composite Materials. Compos Part A 1996;27:1123–31.

[3] Davies GAO, Zhang X. Impact Damage Prediction in Carbon Composite Structures. Int J Impact Eng 1995;16:149–70. https://doi.org/10.1016/0734-743X(94)00039-Y.

[4] Williams G, Trask R, Bond I. A Self-Healing Carbon Fibre Reinforced Polymer for Aerospace Applications. Compos Part A 2007;38:1525–32. https://doi.org/10.1016/j.compositesa.2007.01.013.

[5] Yang R, Yunze H. Optically and Non-optically Excited Thermography for Composites: A review. Infrared Phys Technol 2016;76:26–50. https://doi.org/10.1016/j.infrared.2015.12.026.

[6] Gholizadeh S. A review of non-destructive testing methods of composite materials. XV Port. Conf. Fract., Elsevier; 2016, p. 50–7. https://doi.org/10.1016/j.prostr.2016.02.008.

[7] He Y, Chen S, Zhou D, Huang S, Wang P. Shared excitation based nonlinear ultrasound and vibrothermography testing for CFRP barely visible impact damage inspection. IEEE Trans Ind Informatics 2018;14:5575–84. https://doi.org/10.1109/TII.2018.2820816.

[8] Cartz L. Nondestructive Testing. Milwaukee: ASM International; 1995.

[9] Scott IG, Scala CM. A Review of Non-Destructive Testing of Composite Materials. NDT Int 1982;15:75–86. https://doi.org/10.1016/0308-9126(82)90001-3.

[10] Smith RA, Nelson LJ, Mienczakowski MJ, Wilcox PD. Ultrasonic Analytic-Signal Responses from Polymer-Matrix Composite Laminates. IEEE Trans Ultrason Ferroelectr Freq Control 2018;65:231–43. https://doi.org/10.1109/TUFFC.2017.2774776.

[11] Smith RA, Nelson LJ, Mienczakowski MJ, Challis R. Automated Non-Destructive Analysis and Advanced 3D Defect Characterisation From Ultrasonic Scans of Composites. Insight 2009;51:82–7. https://doi.org/10.1784/insi.2009.51.2.82.

[12] Agyei RF, Sangid MD. A Supervised Iterative Approach to 3D Microstructure Reconstruction from Acquired Tomographic Data of Heterogeneous Fibrous Systems. Compos Struct 2018;206:234–46. https://doi.org/10.1016/j.compstruct.2018.08.029.

[13] Léonard F, Stein J, Soutis C, Withers PJ. The Quantification of Impact Damage Distribution in Composite Laminates by Analysis of X-Ray Computed Tomograms. Compos Sci Technol 2017;152:139–48. https://doi.org/10.1016/j.compscitech.2017.08.034.

[14] Mccombe GP, Rouse J, Trask RS, Withers PJ, Bond IP. X-ray Damage Characterisation in Self-Healing Fibre Reinforced Polymers. Compos Part A 2012;43:613–20. https://doi.org/10.1016/j.compositesa.2011.12.020.

[15] Baaklini Y, Yancey R, Swickard S. Ceramic Matrix Composites Characterization

with X-Ray Microtomography and Ultrasonics. Proc. 17th Annu. Conf. Compos. Adv. Ceram. Mater. Ceram. Eng. Sci. Proc., Hoboken, NJ, USA: John Wiley & Sons, Inc.; 1993, p. 473–84. https://doi.org/10.1002/9780470314180.ch72.

[16] Kim J, Liaw PK. Tensile fracture behavior of Nicalon/SiC composites. Metall Mater Trans A Phys Metall Mater Sci 2007;38 A:2203–13. https://doi.org/10.1007/s11661-007-9306-3.

[17] Olivo A, Speller R. A coded-aperture technique allowing x-ray phase contrast imaging with conventional sources. Appl Phys Lett 2007;91:074106. https://doi.org/10.1063/1.2772193.

[18] Endrizzi M, Diemoz PC, Millard TP, Louise Jones J, Speller RD, Robinson IK, et al. Hard X-Ray Dark-Field Imaging with Incoherent Sample Illumination. Appl Phys Lett 2014;104:3–6. https://doi.org/10.1063/1.4861855.

[19] Revol V, Plank B, Kaufmann R, Kastner J, Kottler C, Neels A. Laminate Fibre Structure Characterisation of Carbon Fibre-Reinforced Polymers by X-Ray Scatter Dark Field Imaging with a Grating Interferometer. NDT&E Int 2013;58:64–71. https://doi.org/10.1016/j.ndteint.2013.04.012.

[20] Astolfo A, Endrizzi M, Vittoria FA, Diemoz PC, Price B, Haig I, et al. Large field of view, fast and low dose multimodal phase-contrast imaging at high x-ray energy. Sci Rep 2017;7:1–8. https://doi.org/10.1038/s41598-017-02412-w.

[21] Cloetens P, Pateyron-Salomé M, Buffière JY, Peix G, Baruchel J, Peyrin F, et al. Observation of Microstructure and Damage in Materials by Phase Sensitive Radiography and Tomography. J Appl Phys 1997;81:5878–86.

https://doi.org/10.1063/1.364374.

[22] Revol V, Jerjen I, Kottler C, Schütz P, Kaufmann R, Lüthi T, et al. Sub-Pixel Porosity Revealed by X-Ray Scatter Dark Field Imaging. J Appl Phys 2011;110:1–5. https://doi.org/10.1063/1.3624592.

[23] Hannesschläger C, Revol V, Plank B, Salaberger D, Kastner J. Fibre Structure Characterisation of Injection Moulded Short Fibre-Reinforced Polymers by X-Ray Scatter Dark Field Tomography. Case Stud Nondestruct Test Eval 2015;3:34–41. https://doi.org/10.1016/j.csndt.2015.04.001.

[24] Gresil M, Revol V, Kitsianos K, Kanderakis G, Koulalis I, Sauer M-O, et al. EVITA Project: Comparison Between Traditional Non-Destructive Techniques and Phase Contrast X-Ray Imaging Applied to Aerospace Carbon Fibre Reinforced Polymer. Appl Compos Mater 2017;24:513–24. https://doi.org/10.1007/s10443-016-9540-1.

[25] Endrizzi M, Murat BIS, Fromme P, Olivo A. Edge-illumination X-Ray Dark-Field Imaging for Visualising Defects in Composite Structures. Compos Struct 2015;134:895–9. https://doi.org/10.1016/j.compstruct.2015.08.072.

[26] Massimi L, Hagen CK, Endrizzi M, Munro PRT, Havariyoun G, Hawker SPM, et al. Laboratory-Based X-Ray Phase Contrast CT Technology for Clinical Intra-Operative Specimen Imaging. Proc. SPIE 10948; 109481R, 2019. https://doi.org/10.1117/12.2511770.

[27] Maughan Jones CJ, Vittoria FA, Olivo A, Endrizzi M, Munro PRT. Retrieval of weak x-ray scattering using edge illumination. Opt Lett 2018;43:3874.

https://doi.org/10.1364/ol.43.003874.

[28] Limaye A. Drishti: a Volume Exploration and Presentation Tool. Proc. SPIE 8506, Dev. X-Ray Tomogr. VIII, 85060X, 2012. https://doi.org/10.1117/12.935640.

[29] Kok MDR, Robinson JB, Weaving JS, Jnawali A, Pham M, Iacoviello F, et al. Virtual unrolling of spirally-wound lithium-ion cells for correlative degradation studies and predictive fault detection. Sustain Energy Fuels 2019;3:2972–6. https://doi.org/10.1039/c9se00500e.

List of Figures:

Figure 1: Photograph of specimen: (a) impact damage on front surface; (b) protrusion on back surface.

Figure 2: Immersion ultrasonic imaging setup.

Figure 3: Experimental EI XPCi CT setup.

Figure 4: Schematic showing the changes in Gaussian shape with (blue) and without (red) sample, used for retrieval of absorption, refraction and scattering signals.

Figure 5: Undamaged area of sample: ultrasonic B-scan with (a) front surface (indent) and (b) back surface (protrusion) facing the transducer (colour scale signal voltage in volts); (c) position of B-scans and cross sections within the sample; cross-section of retrieved X-ray (d) absorption, (e) refraction, (f) scattering CT reconstructions; 3D rendering of the sample for retrieved (g) absorption, (h) refraction, (i) scattering; (j) superposition of the retrieved EI XPCi CT images with absorption (blue), refraction (green), scattering (red).

Figure 6: Delamination: ultrasonic B-scan with (a) front surface (indent) and (b) back surface (protrusion) facing the transducer (colour scale signal voltage in volts); (c) position of B-scans and cross sections within the sample; cross-section of retrieved X-ray (d) absorption, (e) refraction, (f) scattering CT reconstructions; 3D rendering of the sample for retrieved (g) absorption, (h) refraction, (i) scattering; (j) superposition of the retrieved EI XPCi CT images with absorption (blue), refraction (green), scattering (red).

Figure 7: 2-directional cut through 3D rendering showing shape of delamination around the main impact damage in the retrieved X-ray (a) absorption, (b) refraction, and (c) scattering signals.

Figure 8: Center of damage: ultrasonic B-scan with (a) front surface (indent) and (b) back surface (protrusion) facing the transducer (colour scale signal voltage in volts); (c) position of B-scans and cross sections within the sample; cross-section of retrieved X-ray (d) absorption, (e) refraction, (f) scattering CT reconstructions; 3D rendering of the sample for retrieved (g) absorption, (h) refraction, (i) scattering; (j) superposition of the retrieved EI XPCi CT images with absorption (blue), refraction (green), scattering (red); (k) zoom impact damage.

Figure 9: Horizontal profile plots taken across 2D projections of CT retrievals (red line on images) for (a-b) absorption, (c-d) refraction, and (e-f) scattering signals; (g-h) ultrasonic double-through transmission C-scan.

Figure 10: Comparison of crack observed in the sample for (a) low resolution absorption scan; (b) high resolution absorption scan using commercial system; superposition of the high resolution absorption scan with (c) low resolution refraction signal (green) and with (d) low resolution scattering signal (red).

Figure 1

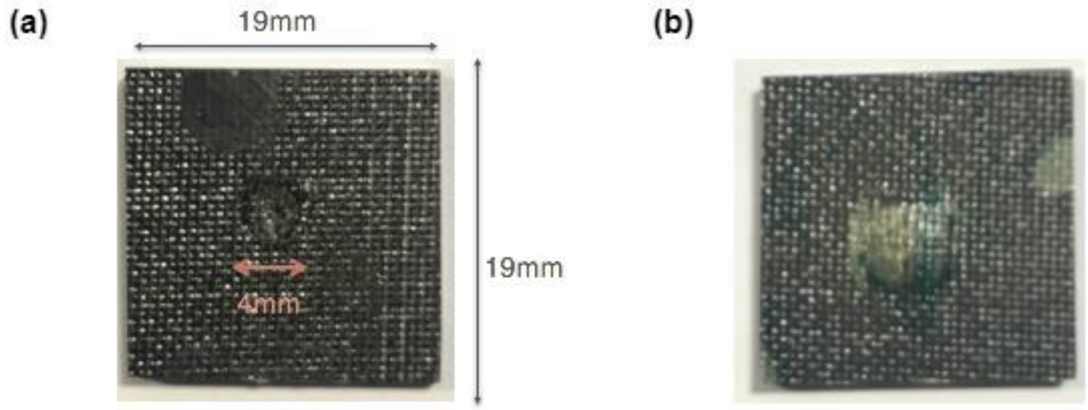

Figure 2

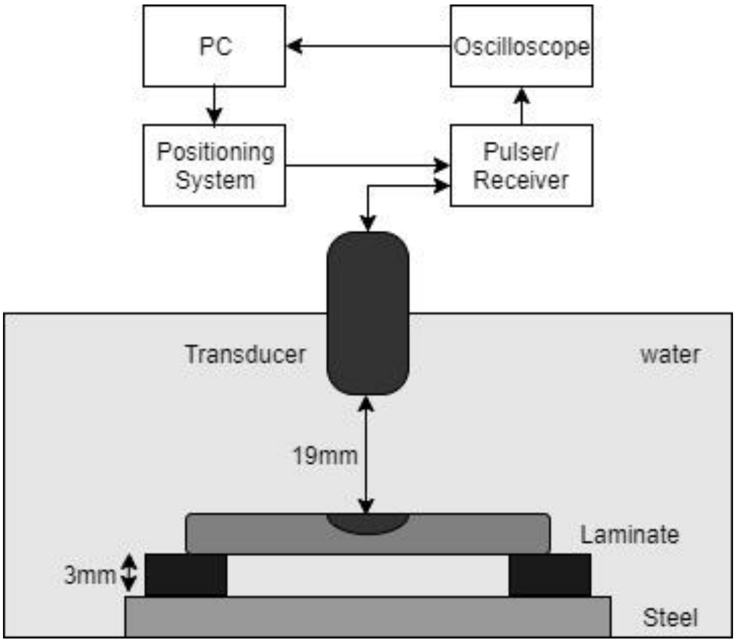
PC
Oscilloscope
Positioning System
Pulser/ Receiver
Transducer
water
19mm
Laminate
3mm
Steel

Figure 3

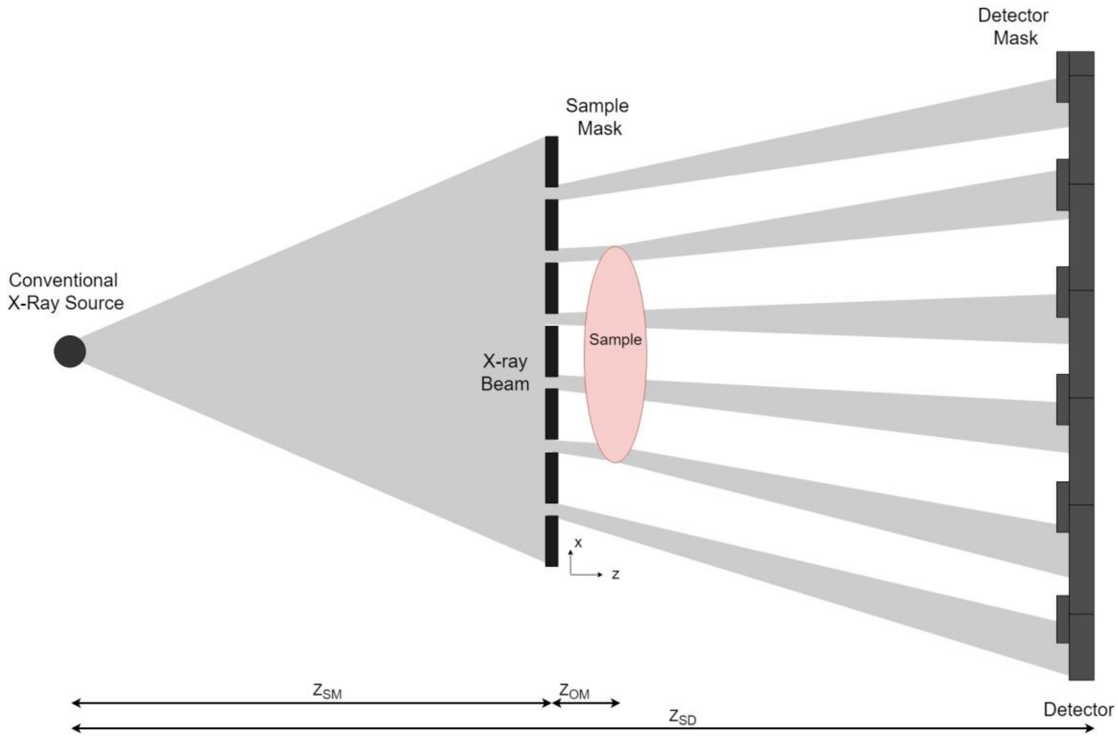
Detector
Mask
Sample
Mask
Conventional
X-Ray Source
Sample
X-ray
Beam
x
z
Z_{SM}
Z_{OM}
Z_{SD}
Detector

Figure 4

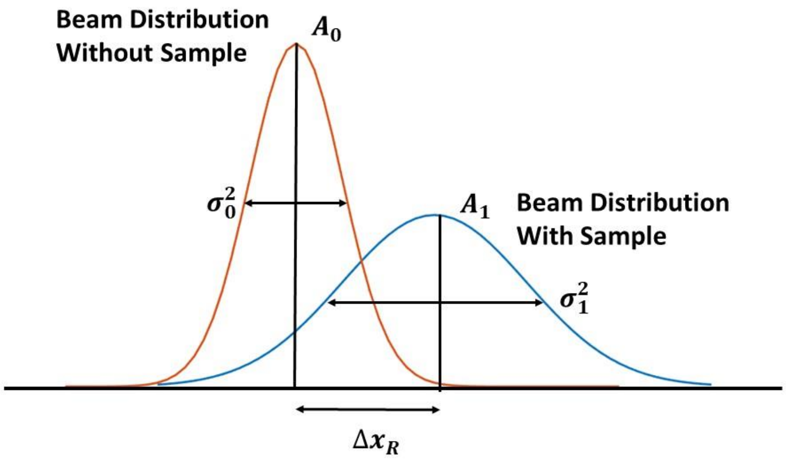
Beam Distribution
Without Sample
A_0
σ_0^2
A_1
Beam Distribution
With Sample
σ_1^2
Δx_R

Figure 5

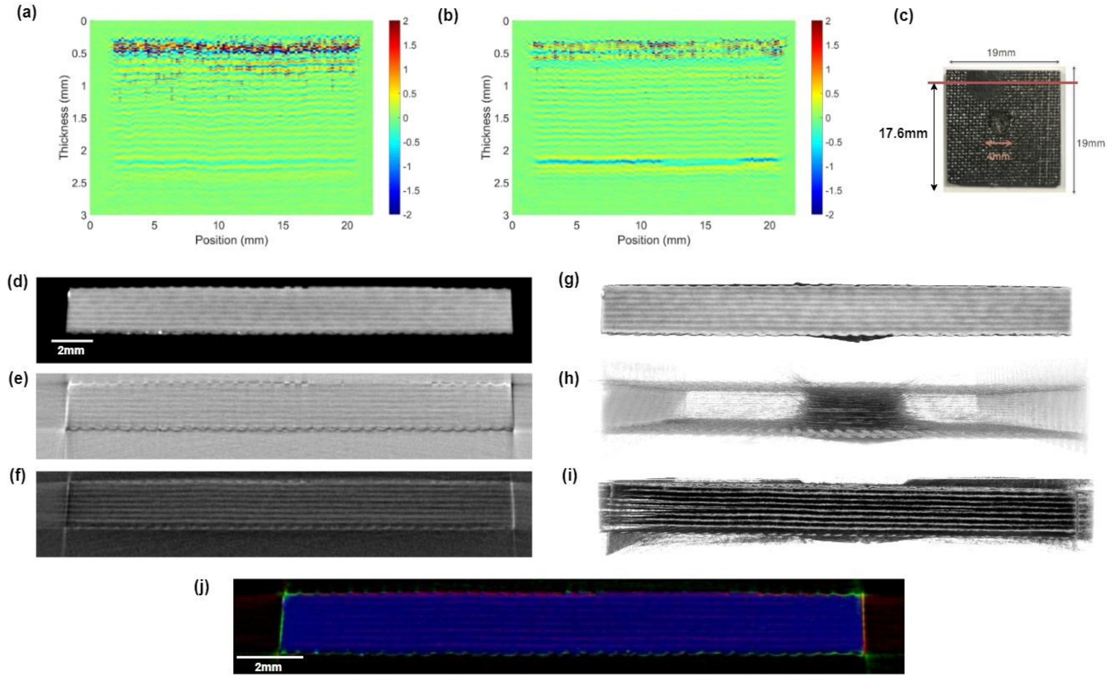
(a)
(b)
(c)
Thickness (mm)
Position (mm)
19mm
17.6mm
19mm
(d)
(e)
(f)
(g)
(h)
(i)
(j)
2mm
2mm

Figure 6

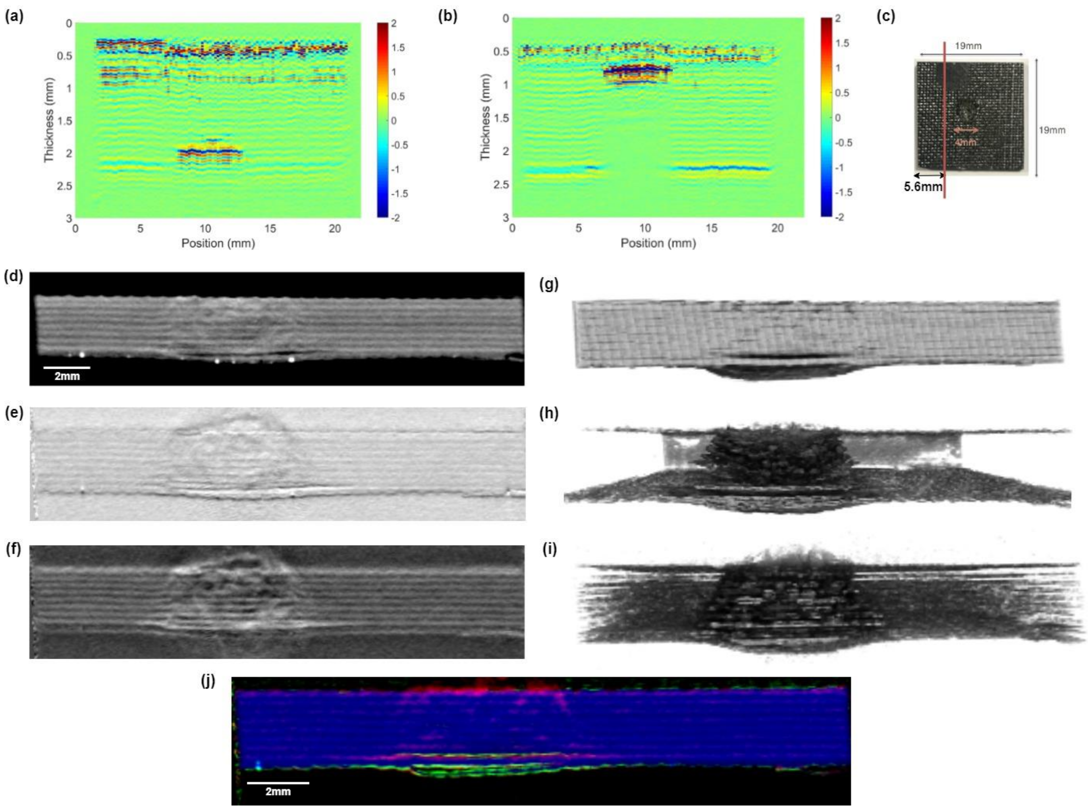

Figure 7

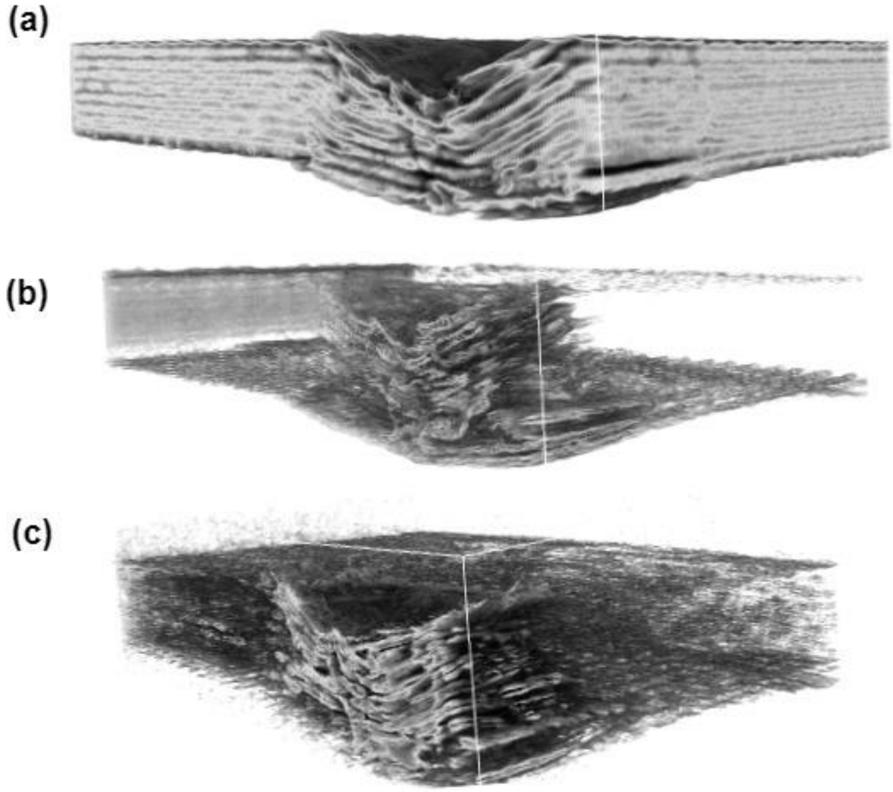

Figure 8

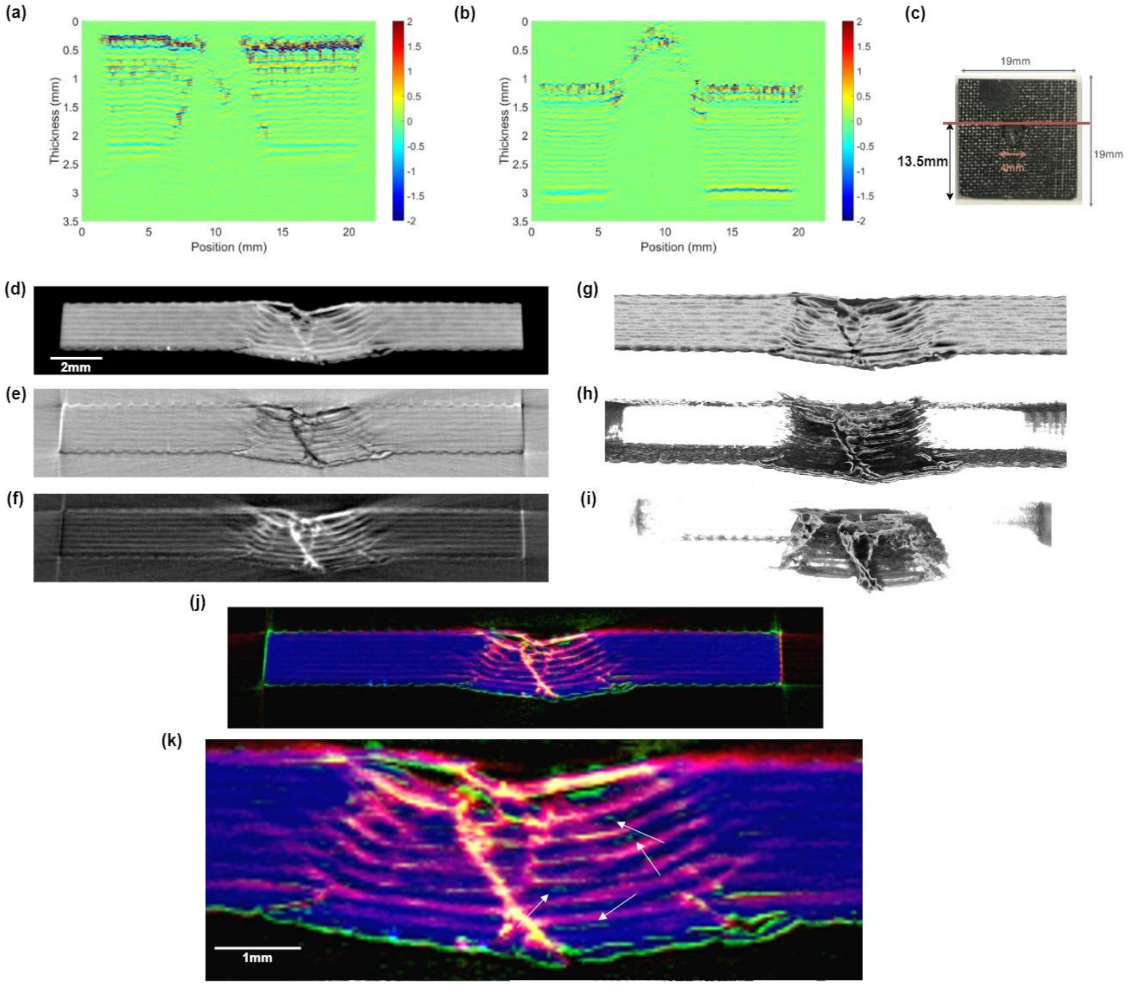

(a)
(b)
(c)
Thickness (mm)
Position (mm)
19mm
19mm
13.5mm
4mm
(d)
2mm
(e)
(f)
(g)
(h)
(i)
(j)
(k)
1mm

521 **Figure 9**

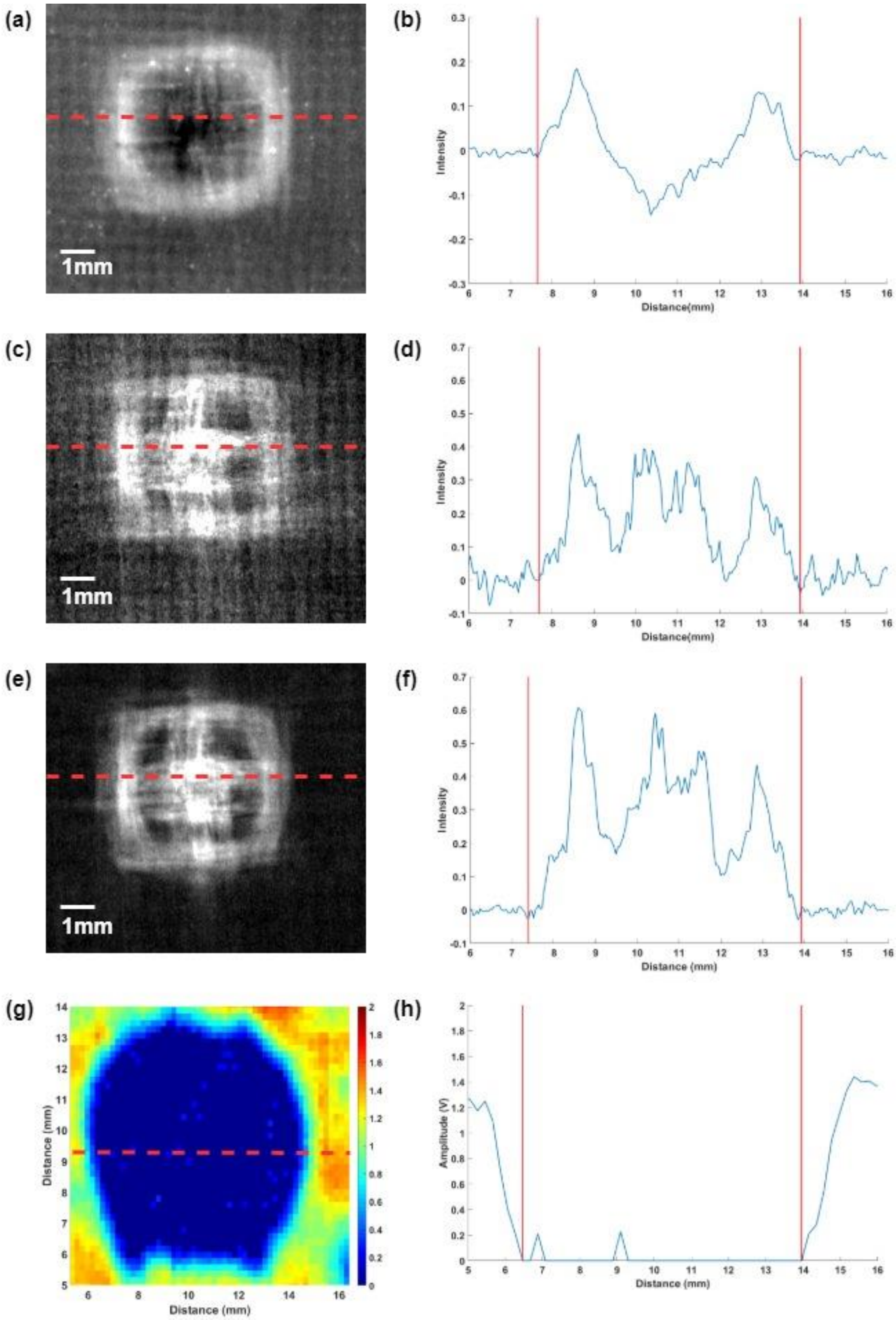

522

523

Figure 10